Ocean Engineering 277 (2023) 114272

Contents lists available at ScienceDirect

Ocean Engineering

journal homepage: www.elsevier.com/locate/oceaneng

Operability analysis of control system for ROV launch-and-recovery from autonomous surface vessel ☆

Celine Tran [a,*], Ivan Gushkov [a,*], Kristoffer Nordvik [a,*], Simen T. Røang [a], Simen B. Lysthaug [a], Babak Ommani [c], Thor I. Fossen [a], Vahid Hassani [c], Vidar Smines [b], Tor A. Johansen [a,*]

[a] Center for Autonomous Marine Operations and Systems, Department of Engineering Cybernetics, Norwegian University of Science and Technology, 7491 Trondheim, Norway
[b] Kongsberg Maritime, Ålesund, Norway
[c] SINTEF Ocean, Trondheim, Norway

ARTICLE INFO

Keywords:
Marine operations
Launch and recovery systems
ROV motion control
Dynamic positioning
First-order wave motion
Hydrodynamic simulation

ABSTRACT

The launch and recovery of equipment such as remotely operated vehicles (ROVs) is a critical task that defines the operability limits of many marine operations. This paper considers the analysis of control systems that are designed to maximize the operability limits for launch and recovery of a ROV from a small unmanned surface vessel (USV). We use numerical simulation for the analysis, where the method combines recent approaches for wave compensating dynamic positioning, active heave compensation, and positioning control of the ROV with multi-body dynamic simulation of the surface vessel and ROV, including hydrodynamic forces and dynamic interactions from wires that depend on the ROV depth and moonpool. The results show that the choice of control algorithms and their tuning parameters has a significant effect on the system's operability, and should be carefully designed and tuned to optimize the operability limits for any given sea state, weather and operational setup. The results show that numerical analysis with a system's simulation is an effective tool to verify operability and its sensitivity to various parameters for the given ROV recovery application.

1. Introduction

Marine operations that involve wire-suspended equipment in the wave zone or close to the seabed are often limited by the wave-induced forces and motions. One example is the launch and recovery of ROVs from a relatively small surface vessel such as the autonomous surface ship concept illustrated in Fig. 1. The relatively small size of the ship implies that its motions are more influenced by the waves than a larger conventional ship in the same sea state would be. As illustrated in Fig. 1, the ROV is not exposed to open water conditions, but its hydrodynamics and motion is strongly coupled to the motion of the surface ship. This results from both the wires and the complex hydrodynamics interaction caused by the moonpool (MP) and proximity to the ship hull, where the ROV is positioned at the lower end of the moonpool during launch and recovery. The dynamics of this multi-body coupled system is also strongly influenced by the automatic control systems, in particular the dynamic positioning (DP) system on the ship, the winch and vertical compensation system, and the active control of the ROV using its thrusters. It is therefore of interest to optimize the design of control systems for maximizing the operability limits, and use numerical simulation for analysis, Anon (2011), Berg et al. (2015).

1.1. ROV launch and recovery

For the operation of ROVs from a small unmanned surface vessel (USV), we have identified that the recovery of the ROV is critical. As illustrated in Fig. 2, there are two phases. First, recovery starts when the ROV is merged with the suspended latchbeam (LB). This is referred to as *latchbeam docking*, see Fig. 2a. Second, the connected ROV-LB object merges with the cursor. This is referred to as *cursor docking*, as illustrated in Fig. 2b. The system that implements this is known as a launch-and-recovery-system (LARS).

In the first phase, the LB is lowered into a depth where there remains only a small effect of surface waves on the water surrounding the ROV, and whereby the LB is largely decoupled from the lateral

☆ This work was supported by the Research Council of Norway, Kongsberg Martime, DOF Subsea and Reach Subsea through the ROV Revolution projects number 296262 and 310166, and the Research Council of Norway, Equinor and DNV through the Centre for Autonomous Marine Operations and Systems (NTNU AMOS), project number 223254.

* Corresponding authors.
E-mail address: tor.arne.johansen@ntnu.no (T.A. Johansen).

https://doi.org/10.1016/j.oceaneng.2023.114272
Received 8 February 2023; Received in revised form 3 March 2023; Accepted 19 March 2023
Available online 28 March 2023

Fig. 1. ROV operated from a relatively small exemplary USV. Courtesy Kongsberg Maritime.

motions of the USV by means of hydrodynamic damping acting on the length of paid out cursor wires. Moreover, in order to further decouple the LB from the USV's wave induced motion at the surface, the vertical motion of the LB is controlled by cursor wire winches onboard the USV with an active heave compensation (AHC) system that will automatically control the payout of the two wires, seeking to largely decouple the latch beam from the vertical motions of the USV. Moreover, the LB can also move in the horizontal plane, as a pendulum guided by the wires, being excited by the wave induced motion of the USV. There will be residual motions due to the lateral motions of the USV, and/or wave induced motions acting on the cursor wires and LB itself. In order to dock the ROV into the LB, the umbilical can also be used for hoisting. In addition, the ROV is assumed to use active control with its thrusters.

In the second stage of recovery, see Fig. 2b, the rigidly connected ROV and LB assembly is being hoisted by the umbilical winch into the cursor frame that is located at the bottom of the moonpool. During this stage heave compensation will not be active, considering the motions of the ROV and USV should be synchronized as much as practically possible, rather than being decoupled. However, due to the complex hydrodynamics near the moonpool and interaction from the ship hull onto the ROV, their motions will not be perfectly synchronized in practice. Therefore, we will study how the ROV motion control system can be used to assist in synchronizing their motion, typically by using the ROV's thrusters to guide the combined object of latchbeam and ROV to follow the motions of the larger USV. We note that the opposite, i.e. USV following the latch beam and ROV could also apply as an alternative or supplement, Halvorsen et al. (2020). However, in the present paper a DP system is used solely for USV station-keeping and to reduce wave-induced motions, Nordvik and Johansen (2022).

1.2. Literature review and contribution

The use of numerical simulations that combine hydrodynamic models with multi-body models and wire models are common, e.g. Guachamin Acero et al. (2016), Acero et al. (2017), Li et al. (2020). Many of the published articles acknowledge that control systems such as DP and heave compensation have an effect on the operability. However, control systems are rarely included in the simulations. Even if they are included, the tuning and optimization of algorithm parameters with their intricate effects are often not considered in detail. On the other hand, it is well known that the choice of control structure, control algorithm and its tuning parameters may have a significant effect on the performance of an actively controlled marine system, e.g. Johansen et al. (2003), Fossen (2021). Moreover, in order to design a suitable control system, our hypothesis is that there is a need to consider all these effects jointly, and the only practical tool that can integrate all these elements appears to be time-domain numerical simulation. In

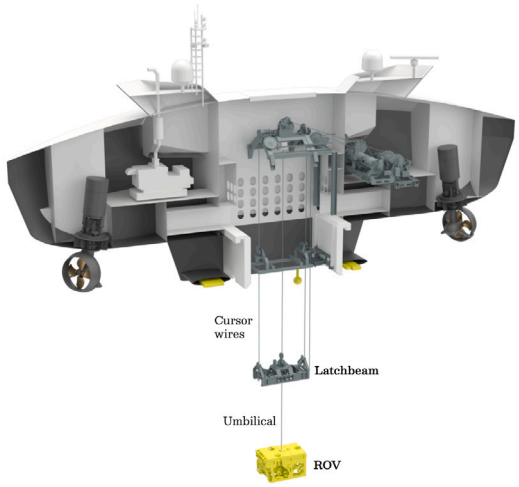

(a) Latchbeam docking: During the initial stage of recovery the ROV (yellow) is docking into the LB that is suspended by two wires. The ROV is connected to the ship via its umbilical that is also used to hoist the ROV into the LB.

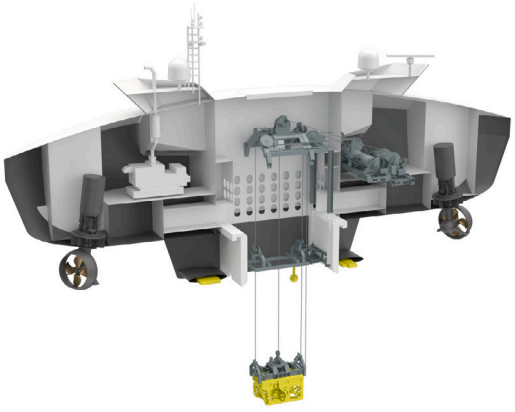

(b) Cursor docking: During the final stage of recovery the ROV is latched to a LB (structure on top of the ROV) that is hoisted up by two wires.

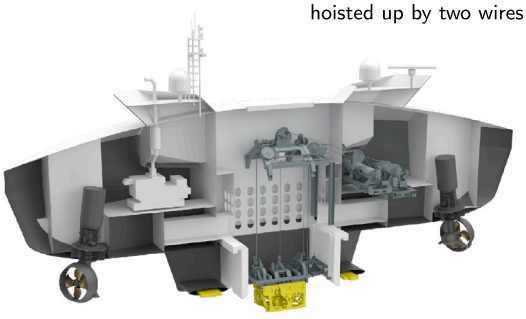

(c) Cursor docking end-state: The LB-ROV assembly is rigidly secured and locked after docking into the cursor (horizontal structure in the lower end of the moonpool).

Fig. 2. ROV launched and recovered from a relatively small exemplary USV and LARS. Courtesy Kongsberg Maritime.

this paper we combine recently developed automatic control methods for wave compensating DP, Nordvik and Johansen (2022) and active control of the ROV, Landstad et al. (2021), with multi-body dynamic simulation of surface vessel, LARS and ROV, including hydrodynamic forces and interactions from wires, Fossen (2021). The main contributions and novelty that also represents extensions compared to our

previous work (Halvorsen et al., 2020; Nordvik and Johansen, 2022; Landstad et al., 2021) are:

- Development and verification of a system model that combines coupled potential flow frequency domain hydrodynamics of the USV and ROV from WAMIT (2020) with rigid-body time-domain simulation using the MSS toolbox in MATLAB/Simulink. Special focus is given on dynamic modeling of fluid memory effects, the influence of ROV and LB depth on the hydrodynamics, wire and umbilical tension, the latchbeam docking scenario, and combined USV and ROV control systems.
- Demonstration of the use of this numerical simulation tool for analysis of operability/workability for (1) docking of ROV in cursor using winch and/or active control of ROV in a range of sea states and headings, (2) active control of ROV for latchbeam docking at various depths and sea states.

We emphasize that the objective of this paper is *not* to provide a systematic design and analysis of the control systems, but to illustrate by examples how the numerical analysis using simulation can be used to study details on how control system algorithms and their tuning parameters will influence the operability limits of ROV recovery.

1.3. Paper structure

The paper is organized as follows. In Section 2 we introduce the models used in the numerical simulation framework. The automatic control systems under investigation is summarized in Section 3. Results from numerical simulations and discussion of these results are provided in Section 4, before conclusions are given in Section 5.

2. Method

This section describes the numerical simulation tool. In particular, the modeling of the USV, ROV and LARS is presented.

2.1. Model structure

The system structure for the latchbeam docking simulations, when the ROV and LB are not rigidly connected as in Fig. 2a, is illustrated in Fig. 3.

The dynamic model includes the USV, ROV and LB which are modeled separately, each in 6 degrees-of-freedom with generalized position vector $\boldsymbol{\eta} \in \mathcal{R}^6$ containing linear positions in a local North-East-Down (NED) coordinate system and Euler angles $\boldsymbol{\Theta} = (\varphi, \theta, \psi)^T$ describing the attitude, as well as generalized velocity vector $\boldsymbol{\nu} \in \mathcal{R}^6$ containing the linear velocities and angular rates in a body-fixed coordinate system (BODY). The main forces acting on each of the bodies are

- Ocean current force $\boldsymbol{\tau}_{current} \in \mathcal{R}^6$ that is rotated from the NED frame to the body-fixed frame.
- Wave forces $\boldsymbol{\tau}_{wave} \in \mathcal{R}^6$ affecting the respective bodies obtained from WAMIT computations of the first order wave force transfer functions as well as the irregular wave spectra with directional spreading defined by the sea state and operating area.
- Wind forces $\boldsymbol{\tau}_{wind} \in \mathcal{R}^6$ affecting the USV.
- Hydrodynamic added mass, potential flow damping and restoring forces are obtained from WAMIT. The fluid memory effects are included using retardation functions, Cummins (1962), and additional linear and quadratic viscous forces are modeled based on available experimental studies in model scale. The piston mode resonant flow inside the moonpool is modeled using the so-called lid method, Ommani et al. (2018). Doing so, the effect of moonpool response on hydrodynamic forces on the ROV and LB is considered. Due to large differences in mass, the effect of LB and ROV on the USV is neglected. Coupling effects between the ROV and LB are considered to be neglectable in latchbeam docking, and therefore not included.
- Wire forces $\boldsymbol{\tau}_w \in \mathcal{R}^6$ between the winch and the LB, including heave compensation system.
- Umbilical forces $\boldsymbol{\tau}_u \in \mathcal{R}^6$ between the winch and the ROV, and may also affect the latchbeam.
- Control forces on the USV (thrust $\boldsymbol{\tau}_{DP} \in \mathcal{R}^6$) in the horizontal plane), ROV ($\boldsymbol{\tau}_{ROV,control} \in \mathcal{R}^6$) and heave compensation system ($\boldsymbol{\tau}_{cursor,winch}$).

The system structure for cursor docking is similar, except that the model is reduced to simulate the ROV and LB as one single (connected) rigid body with lumped scaled mass and damping according to the dimensions. With the ROV and LB being connected mechanically, the umbilical has no tension since they are both suspended by the two cursor wires. The models are gathered in a matrix–vector form resulting in system matrices with dimensions $6n \times 6n$, where n is the number of bodies, i.e. $n = 2$ when the ROV is rigidly connected to the LB (cursor docking), and $n = 3$ when they move separately (LB docking).

2.2. WAMIT and MATLAB MSS toolbox

WAMIT uses 3D potential flow theory to solve a boundary value problem satisfying the Laplace equation in the fluid domain, with linearized free surface and body boundary conditions. The problem is solved by discretizing the body surface into panels and satisfying the body boundary condition at the center, hence it is often referred to as a panel method. The size and number of panels will correspond to the discretization of the solution obtained, where more intricate shapes require more panels, Faltinsen (1990), WAMIT (2020). The result of the WAMIT calculations are

- Hydrodynamic added mass and potential damping as frequency dependant coefficients.
- First- and second-order wave-load transfer functions.
- Retardation functions - fluid-memory effects.

WAMIT also solves the boundary value problem for zero and infinite added mass. This is useful for developing a time domain model of the radiation forces because it requires integration from zero to infinite frequency as described in Cummins (1962) and Fossen and Perez (2008).

The hydrodynamic coupling from the hull and the moonpool to the LB and ROV changes significantly with the vertical distance between the moonpool inlet and the LB and ROV. A quasi-steady approach is adopted for modeling this effect, which is more consistent when the time scale of ROV's depth change is much larger than wave induced motions. WAMIT calculations are therefore repeated for every 1 meter depth interval from the ROV/LB being at the moonpool inlet until it is 18 meters below this point. The individual WAMIT data from each depth are then selected depending on the ROV/LB depth. This also implies that the fluid memory effect identification process described in Section 2.4 must be conducted for every depth. The obtained state space representation of the different WAMIT-based fluid memory models did not have the same system order, and a depth-continuous simulator-model based on interpolation was deemed difficult. Instead a simulator with a fixed fluid memory dynamics model was used for the simulations at discrete depths, which was implemented with a switching of model parameters for every meter depth as the ROV approaches the USV.

To utilize the hydrodynamic data obtained by WAMIT for time-domain simulation, the MATLAB/Simulink-based toolbox MSS (Fossen and Perez, 2004) is used. This toolbox can be used to transform the WAMIT data to a data structure (vessel-structure) in MATLAB containing the system matrices and wave force transfer functions represented in the NED coordinate frame, as the WAMIT data is represented in a different frame. This leads to a time-domain simulation framework as illustrated in Fig. 3. A model from the MSS toolbox is also used to generate time-domain realizations for short-crested sea states based on the JONSWAP spectrum, and wind forces according to the NORSOK spectrum.

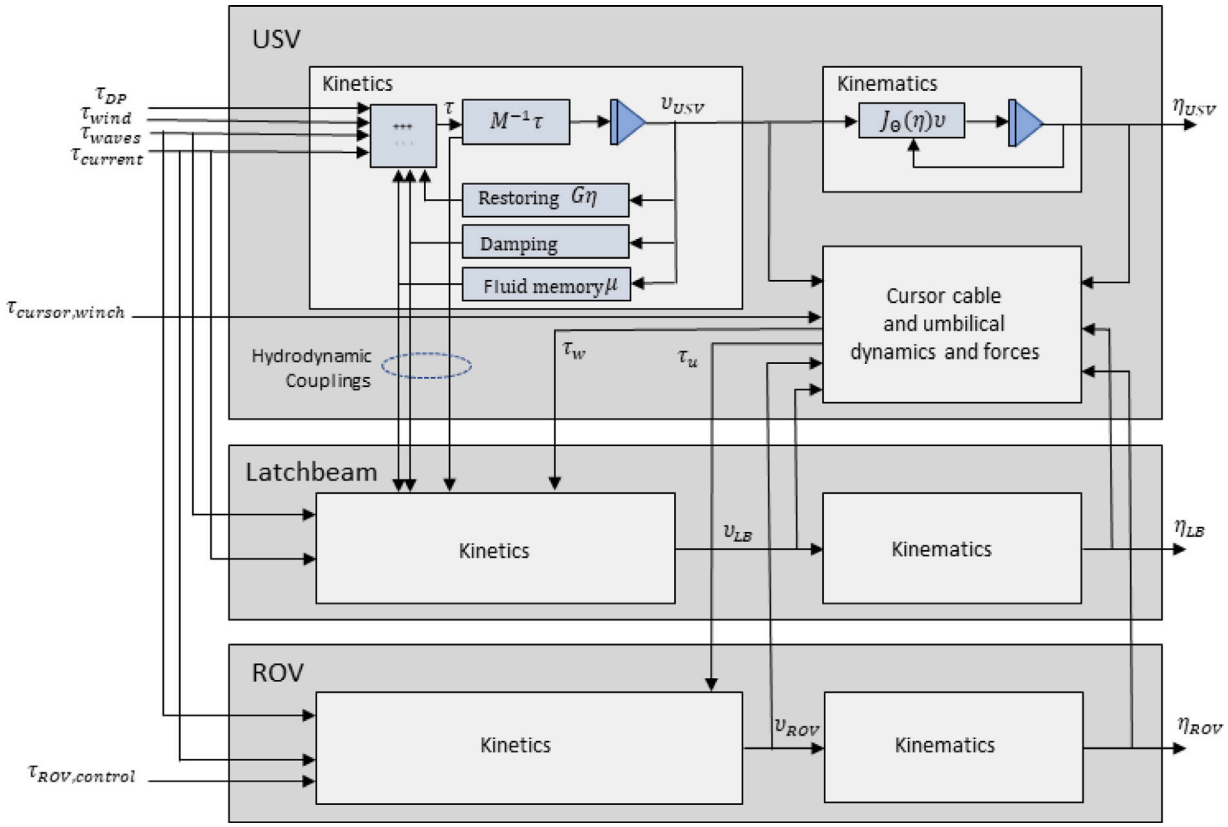

Fig. 3. Block diagram open loop system model of USV, latchbeam, ROV, cursor wires and umbilical.

Table 1
Physical properties of the USV, moonpool (MP), LB and ROV.

	USV	MP	LB	ROV
Mass (m)	162668 kg	N/A	1800 kg	2000 kg
Length (L_{pp})	24 m	5 m	2.15 m	2.15 m
Beam (B)	7.5 m	2.8 m	1.2 m	1.2 m
Draft (T)	4.1 m	4.1 m	0.5 m	1.2 m

Table 2
Position of CG and CB relative to CO [m], for each vessel/body.

$[x^b, y^b, z^b]$	USV	LB	ROV	LB/ROV
p^b_{CG}	[0, 0, −0.16]	[0, 0, 0]	[0, 0, 0]	[0, 0, −0.60]
p^b_{CB}	[0, 0, 2.39]	[0, 0, 0]	[0, 0, 0]	[0, 0, 0]

2.3. Multibody model

The main dimensions of the vessels are given in Tables 1 and 2. In this section we describe how the simulation model is setup.

2.3.1. USV

As the USV hull shown in Fig. 1 has port/starboard and fore/aft symmetry, the system matrices have elements on the diagonal, with coupling-terms off the diagonal in surge/pitch and sway/roll. The total mass matrix $\boldsymbol{M} = \boldsymbol{M}_{RB} + \boldsymbol{M}_A$ consist of the rigid body mass matrix $\boldsymbol{M}_{RB}$ in addition to the infinite-frequency added mass matrix $\boldsymbol{M}_A$ from WAMIT.

The damping forces are given by linear and quadratic terms $\boldsymbol{D}\boldsymbol{v} + \boldsymbol{d}(\boldsymbol{v})\boldsymbol{v}$ with the damping matrix $\boldsymbol{D} = \boldsymbol{D}_P + \boldsymbol{B}_V$. Linear potential damping at infinite frequency $\mathbf{D}_P = \mathbf{B}(\infty)$ from WAMIT is included by adding it to the linear viscous damping matrix $\mathbf{B}_V$.

The damping model was obtained by tuning according to model test data based on 1/8.6 scale experiments done in SINTEF Ocean's basin. To obtain restoring/stiffness in surge, sway and yaw a mooring system was used in model tests. The model includes a linear and a quadratic term with coefficient matrices. Coefficients from the linear model of restoring forces is included in the diagonal restoring matrix $\boldsymbol{G}$. Moreover, two 500 kW azimuth thrusters were assumed, with a diameter of 1.9 m, a bollard pull thrust of 117 kN, and dynamic response as given in Nordvik and Johansen (2022).

2.3.2. ROV

The ROV model is a solid cuboid with dimensions given in Table 1. According to Table 2, the Center of Origin (CO) and Center of Gravity (CG) coincide and the rigid body mass matrix is diagonal. The Center of Buoyancy (CB) and CO also coincide, which results in no restoring moments in roll and pitch. The ROV is fully submerged and neutrally buoyant, hence there will be no restoring forces from buoyancy in heave. The hydrodynamic radiation forces from WAMIT including added mass and potential damping have the same port/starboard and fore/aft symmetry configuration as the USV, but with very small couplings.

The linearized viscous damping is estimated according to a mass-damper equation in surge, sway, heave and yaw with time constants $T_{ROV} = 5$ s, and according to a mass–spring-damper equation in roll and pitch with relative damping ratios, $\zeta_{roll} = 0.5$ and $\zeta_{pitch} = 0.8$. There are no restoring forces or moments on the ROV resulting in $\boldsymbol{G} = \boldsymbol{0}$.

Nonlinear damping is included as quadratic drag functions for the translational motions. The rotational motions are assumed to be small, and linear damping is assumed sufficient. The drag coefficient C_d is uniform for all axes of the ROV since it is modeled as a cuboid. The drag coefficient $C_d = 2.5$ was provided by DNV recommended practice for operability analysis (Anon, 2011).

The ROV has a thruster system which is described in Landstad et al. (2021), and summarized here. It is configured with 11 fixed thrusters. The assumed propeller is the Ka-470 with a diameter of 254 mm and

has a 19 A nozzle. The thrusters have a saturation on rotational speed which is set to match the thrust force that is necessary for the ROV to reach its desired maximum surge velocity of 6 knots, causing its thrusters to be capable of delivering significant thrust force. The shaft speed controller of the electrical motor is tuned to yield a ramp time of approximately 2.5 s. It is modeled as a first order dynamic response with a time-constant of approximately 1.0 s and a time-delay of 0.1 s.

2.3.3. Latchbeam

The LB model is similar to the ROV, with scaled hydrodynamic effects due to the smaller vertical dimension. The radiation forces are scaled only in surge, sway and yaw as the smaller draft will mainly affect these DOFs. These forces are scaled linearly according to the proportion between the ROV and LB with a factor $k = T_{LB}/T_{ROV}$. The factor k is based on the assumption that the hydrodynamic effects are pressure forces that scale linearly with the lateral and frontal areas of the ROV when LB is far from free surface. This applies to the potential damping and added mass.

The LB does not have any linear restoring forces in terms of buoyancy since its not floating or moored, hence $\boldsymbol{G} = \boldsymbol{0}$. Since its not neutrally buoyant, a gravity force must be included. It is modeled as a nonlinear force $\boldsymbol{g}(\boldsymbol{\eta})$ depending on the orientation of the LB. As CG for the LB is located 0.25 m below the attachment point of the wires, gravity will have a restoring effect. This force enters the model together with the wire forces τ_w as an external force, see Section 2.5. The LB has nonlinear damping similar to the ROV.

2.3.4. Connected ROV and latchbeam

The coupled ROV-latchbeam object is modeled by merging the individual models for the ROV and LB, with slight modifications and simplifications. The rigid body mass matrix is calculated from the dimensions obtained from placing the latchbeam on top of the ROV, resulting in a new CG and a larger height. The hydrodynamic body matrices and the fluid memory effects are assumed to be the same as for the ROV, since it is largest.

2.3.5. Coupling terms

The coupling terms from the WAMIT computations includes frequency dependent radiation forces and fluid memory effect models. Additionally, the added mass and potential damping matrices include coupling terms. The coupling effects from the USV to the LB and ROV are included, while the opposite couplings are negligible and not included. A linearized model of moonpool is included in the couplings using the lid method, where responses of the moonpool in the studied sea states are considered in linearization.

2.4. Fluid-memory effects

To implement the retardation functions resulting from WAMIT computations in a time-domain simulation, these functions and Cummin's equation should be approximated by a linear time-invariant state-space model, (Cummins, 1962; Kristiansen et al., 2006):

$$\dot{\boldsymbol{x}} = \hat{\boldsymbol{A}}\boldsymbol{x} + \hat{\boldsymbol{B}}\dot{\boldsymbol{\xi}} \tag{1}$$

$$\boldsymbol{\mu} = \hat{\boldsymbol{C}}\boldsymbol{x} \tag{2}$$

where the vector $\dot{\boldsymbol{\xi}} = [\boldsymbol{v}^b_{sb}, \boldsymbol{\omega}^b_{sb}]^T$ represents the perturbed (seakeeping) translation and rotational velocities in 6 DOFs, $\boldsymbol{\mu} \in \mathcal{R}^6$ is the vector of radiation forces, $\boldsymbol{x}$ is the internal state of the model, and the system matrices $\hat{\boldsymbol{A}}, \hat{\boldsymbol{B}}, \hat{\boldsymbol{C}}$ are found as described below. This state-space representation corresponds to the following transfer function matrix in the frequency domain:

$$\hat{\boldsymbol{K}}(j\omega) = \hat{\boldsymbol{C}}(j\omega\boldsymbol{I} - \hat{\boldsymbol{A}})^{-1}\hat{\boldsymbol{B}} \tag{3}$$

This representation is used in the search for a parametric representation of the retardation functions, that are given as frequency domain data from WAMIT in terms of a finite number of samples of the transfer functions for selected frequencies. A model for each element i, k of the matrix $\hat{\boldsymbol{K}}(j\omega) \in \mathbb{R}^{6\times6}$ can be expressed as

$$\hat{K}_{ik}(s) = \frac{s^l(p_m s^m + p_{m-1}s^{m-1} + \cdots + p_0)}{s^n + q_{n-1}s^{n-1} + \cdots + q_0} \tag{4}$$

The function should have relative degree 1, Fossen and Perez (2008), hence the polynomial order satisfies $n = m + l + 1$. Identification of the polynomial coefficients p_i and q_i are posed as nonlinear curve-fitting problems based on the frequency domain data, and can be solved by using the MATLAB function **invfreqs.m** which uses result of the linearized problem (Levy, 1959) as an initialization for the Gauss–Newton algorithm (Fossen and Perez, 2008) in the Frequency-domain Identification (FDI) toolbox. The transfer function (4) is of order $n = 2$ or greater. In the FDI toolbox the order is first selected automatically, with the option to modify it manually afterwards. Because of the complex multi-body system with interactions to the ROV/LB being close to the moonpool, many of the transfer functions require order higher than 2 to get a good approximation. Our experience is that the results from FDI toolbox requires careful validation and some manual choices and considerations. For example, stability is not included as a constraint in the optimization problem and is not guaranteed. Therefore, stability properties of the obtained model must be analyzed before accepting it. Several of the models first came out with poles and zeros at high frequencies, where the fast dynamics are problematic for numerical integrators. These modes appear to be artifacts of the FDI toolbox, since they appear at frequencies much higher than the frequencies provided by the WAMIT data. Such high frequency dynamics were suppressed by first extending the model with a low-pass filter with cutoff frequency well above the highest frequencies from which we have WAMIT data, and subsequently reducing the order of the filtered model e.g. by balanced realization as proposed in Kristiansen et al. (2006). Effectively, we have found this to remove the spurious high-frequency modes.

Fig. 4 gives an example, where WAMIT data is compared to a stable model for mode $\{3, 3\}$, which corresponds to the direct heave-heave mode for the USV. The jonswap-spectrum for an intermediate sea-state is included to illustrate the most relevant frequencies for the radiation force models. The model quality is evaluated by looking at the added mass and potential damping corresponding to the estimated convolution model, Perez and Fossen (2009). Comparing it to the WAMIT data, the approximate model is matching the WAMIT data well at the wave frequencies, which is highlighted in the plot.

2.5. Wire and umbilical forces

In this section we model the forces from the cursor wires on the LB or LB-ROV assembly, as well as the forces from the umbilical on the ROV.

2.5.1. Gravity

The LB does deliberately not have added buoyancy to make it neutrally buoyant like the ROV. For this reason, a force from gravity will work on the LB. When the ROV and LB are connected, this gravity force will also induce moments on the connected LB-ROV body. This force will work in the CG of the LB, and the wire tension will correspond to the weight of the LB in water. The latchbeam is assumed to consist purely of steel, which has a density of $\rho_{steel} \approx 7900$ [kg/m^3]. This yields the following gravity force when accounting for the displaced water (buoyancy)

$$\begin{aligned} \boldsymbol{F}^n_g &= \left(\boldsymbol{R}^b_n\right)^T [0, 0, f_g]^T \\ f_g &= m_{LB}\, g \left(1 - \frac{\rho_{water}}{\rho_{steel}}\right) = 15.4 \text{ kN} \end{aligned} \tag{5}$$

where $\boldsymbol{R}^b_n$ is the rotation matrix from the NED to the body-fixed coordinate frame. The resulting total force and moments are

$$\boldsymbol{\tau_g} = \begin{bmatrix} \boldsymbol{F}^n_g \\ \boldsymbol{r}^b_{bg} \times \boldsymbol{F}^n_g \end{bmatrix} \tag{6}$$

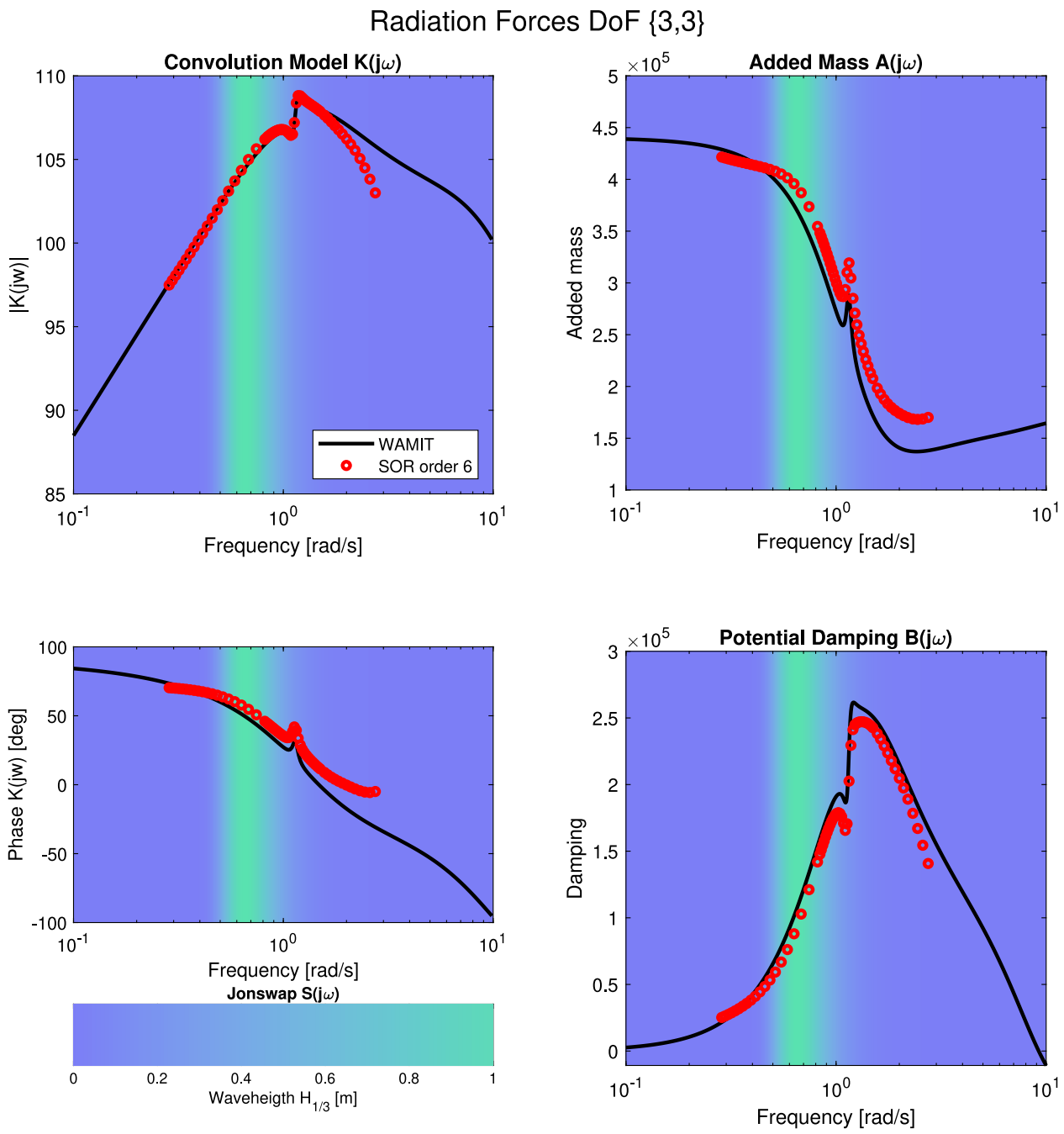

Fig. 4. Example of identified frequency domain model. The red marks are WAMIT data points, the black line is the approximate model, while the green area indicate typical ocean wave frequencies.

where $\boldsymbol{r}_{bg}^{b}$ is the location of CG relative to the CO expressed in the body-fixed frame. For cursor docking with an interconnected ROV and LB this will be nonzero, resulting in the gravitational acceleration working on the LB also inducing moments.

2.5.2. Cursor wire forces

Hydrodynamic forces on the wires connecting the USV and the latchbeam were added using the Morrison equation, e.g (Journée and Massie, 2001). The inertial term in the Morrison equation was neglected as a result of the high Keulegan–Carpenter number (Journée and Massie, 2001) resulting in quadratic damping models.

The LB and ROV are modeled as described in Section 2.3, with the wires connected in the top-center line of the cuboid, parallel with the point of action for the wires on the USV. On the USV, the wires are connected with the point of action for the wires located at either end of the cursor on the LARS. See Table 3 for details about the wire connections represented in body frame.

Table 3
Position of the wire connections (point of action) for the USV and latchbeam.

wire nr i	Position USV $\boldsymbol{p}_{w_{i,USV}}$ [m]			Position latchbeam $\boldsymbol{p}_{w_{i,LB}}$ [m]		
	$x_{w_{i,USV}}$	$y_{w_{i,USV}}$	$z_{w_{i,USV}}$	$x_{w_{i,LB}}$	$y_{w_{i,LB}}$	$z_{w_{i,LB}}/z_{w_{i,RL}}$
Front wire (1)	1.140	0	1.920	1.140	0	−0.25/0.85
Back wire (2)	−1.140	0	1.920	−1.140	0	−0.25/0.85

The wires will work on the LB with a force F, directed at the wire point of action on the cursor as illustrated in Fig. 5. Each wire

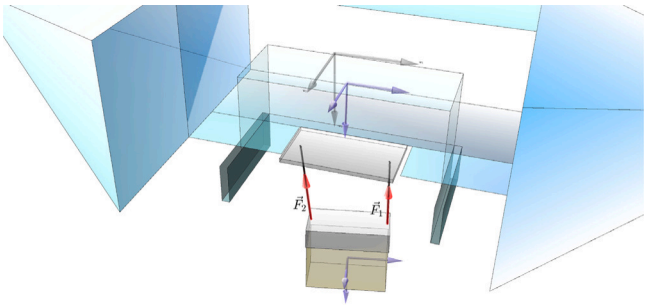

Fig. 5. Illustration of wire forces working on the latchbeam.

is modeled as a "one-way" spring-mass-damper system, neglecting negative tension, i.e. compression:

$$\underbrace{m\ddot{\xi}}_{F} + d\dot{\xi} + k(\xi - \xi_0) = 0 \tag{7}$$

where for $F > 0$

$$F = -(d\dot{\xi} + k(\xi - \xi_0)) \tag{8}$$

Here ξ_0 is the nominal length of the cursor wire (assumed given), while ξ is the actual length considering elasticity. Negative tension from the equation is neglected in this model because there is no pushing force to the latchbeam as in a standard spring-mass-damper system. The tension is still monitored in the simulations as this situation will correspond to slack in the wires, the avoidance of which is an important criterion in the operability analysis, Anon (2011).

For each wire, there is one connection point on top of the latchbeam ($\boldsymbol{p}^b_{w_{i,lb}}$) and one connection point for the USV ($\boldsymbol{p}^b_{w_{i,usv}}$), where

$$\boldsymbol{p}^b_{w_{i,USV}} = [x_{w_{i,USV}}, y_{w_{i,USV}}, z_{w_{i,USV}}]^T \tag{9}$$

$$\boldsymbol{p}^b_{w_{i,LB}} = [x_{w_{i,LB}}, y_{w_{i,LB}}, z_{w_{i,LB}}]^T \tag{10}$$

In general, for wire i and vessel body $v \in \{\text{USV}, \text{LB}\}$, we have:

$$\boldsymbol{p}^n_{w_{i,v}} = \boldsymbol{p}^n_b + \boldsymbol{R}^n_b \boldsymbol{p}^b_{w_{i,v}} \tag{11}$$

$$\boldsymbol{p}^n_{REL_i} = \boldsymbol{p}^n_{w_{i,lb}} - \boldsymbol{p}^n_{w_{i,usv}} \tag{12}$$

$$\xi = \| \boldsymbol{p}^n_{REL_i} \|_2 \tag{13}$$

The velocities in NED for the two wire connection points are expressed from the kinematic equations (Fossen, 2021). Since the wire attachment points are not in the center of the body frame, the velocity due to rotation must also be included, where $\boldsymbol{r}^b_{w_i}$ is the position vector of the wire attachment point in the body frame:

$$\dot{\boldsymbol{p}}^n_{w_{i,v}} = \boldsymbol{R}^b_n(\boldsymbol{v}^b_v + \boldsymbol{\omega}^b \times \boldsymbol{r}^b_{w_i}) \tag{14}$$

$$\dot{\boldsymbol{p}}^n_{REL_i} = \dot{\boldsymbol{p}}^n_{w,lb} - \dot{\boldsymbol{p}}^n_{w_i,usv} \tag{15}$$

Here $\boldsymbol{\omega}^b$ is the corresponding vector of angular rates.

To find the velocity-component parallel with the wire, the relative velocity vector is represented in a frame with one basis vector parallel to the line between the two connection points,

$$\boldsymbol{p}^n_{REL_i} = \begin{bmatrix} p^n_x \\ p^n_y \\ p^n_z \end{bmatrix} \tag{16}$$

where

$$\phi = \tan^{-1}\left(\frac{p^n_y}{p^n_x}\right), \quad \theta = \tan^{-1}\left(\frac{\sqrt{(p^n_x)^2 + (p^n_y)^2}}{p^n_z}\right) \tag{17}$$

The rotation matrix rotating the Down basis-vector (z^n) to $\boldsymbol{p}^n_{REL_i}$ is $\boldsymbol{R}^n_{w_i} = \boldsymbol{R}_{z,\phi}\boldsymbol{R}_{y,\theta}$, where $\boldsymbol{R}_{z,\phi}$ and $\boldsymbol{R}_{y,\theta}$ represent principal rotations

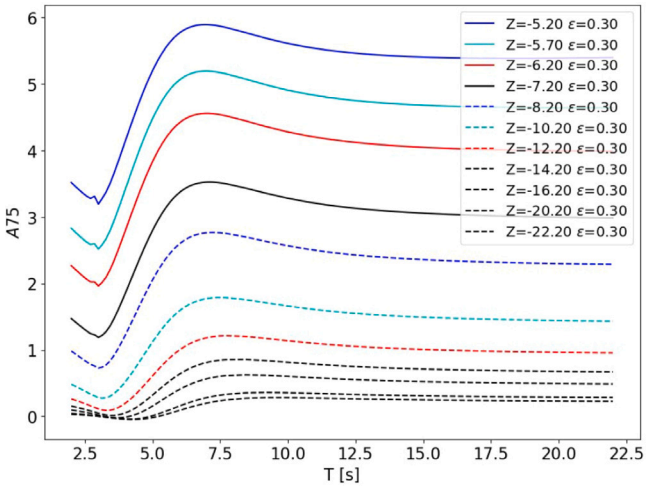

Fig. 6. The added mass for the ROV's surge (7th DOF in the model) coming from the USV's pitch (5th DOF in the model), with curves for multiple depth cases. Z is the coordinate of the ROV center with $Z = 0$ being the mean free surface, and ε is the selected linearized damping coefficient for moonpool lid. T is the wave period.

about the z and y axis, respectively. This yields the following expression for the relative velocities in this "wire-frame" $\{w_i\}$

$$\dot{\boldsymbol{p}}^{w_i}_{REL_i} = (\boldsymbol{R}^n_{w_i})^T(\phi, \theta)\dot{\boldsymbol{p}}^n_{REL_i} = \begin{bmatrix} \dot{p}^{w_i}_x \\ \dot{p}^{w_i}_y \\ \dot{p}^{w_i}_z \end{bmatrix} \tag{18}$$

and the velocity $\dot{\xi}$, which is the z-component of this velocity

$$\dot{\xi} = \dot{p}^{w_i}_z \tag{19}$$

Summarized, the general force model for wire i becomes

$$F_{w_i} = -d\dot{p}^{w_i}_z - k(\| \boldsymbol{p}^n_{REL_i} \| - \xi_0) \tag{20}$$

Tuning of the spring-mass-damper system is done under the assumption of a natural frequency of 10 Hz ($\omega_0 = 20\pi$ rad/s), damped with a relative damping factor $\zeta = 0.1$. For a spring-mass-damper the following relations for a second-order system hold:

$$k = m\omega_0^2 \ , \ d = 2m\zeta\omega_0 \tag{21}$$

where m is the mass. Ideally this spring-mass-damper should be tuned stiffer, but this comes with the cost of simulation efficiency. Thus, a slightly more conservative tuning is chosen, with the wires being elastic to some degree. This approximation has little impact on the simulation results since the dominant ocean wave frequencies are orders of magnitude smaller.

2.6. Model validation

The USV, LB and ROV motions are expected to be increasingly decoupled when the ROV is deeper, for two main reasons:

- Reduced direct excitation of LB, ROV-LB and ROV by waves, due to diminishing particle motions at depth.
- Increasing lateral decoupling of LB or ROV-LB due to increasing pendulum distance, thus diminishing the transmission of lateral forces from the USV via cursor wires onto the LB or LB-ROV, as well as increasing cursor wire damping (whereas vertical decoupling is mainly by AHC), and

For example, Figs. 6 and 7 show the added mass for ROV in surge and heave due to USV pitch and heave motions, respectively. The figures indicate that there is a coupling in these DOFs, and the effects become weaker with increased ROV depth.

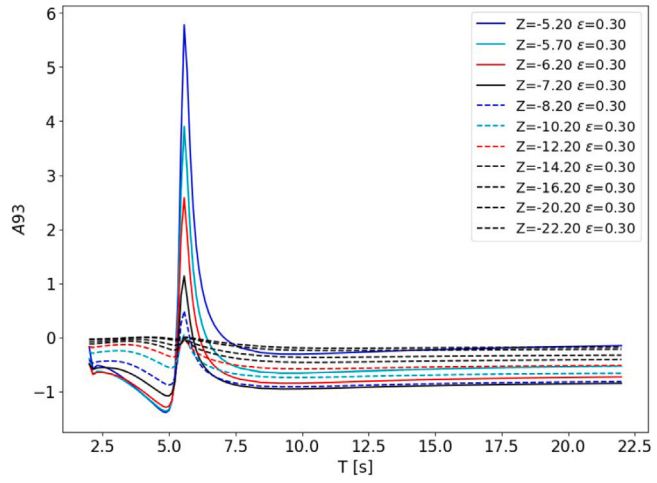

Fig. 7. The added mass for the ROV's heave (9th DOF in the model) coming from the USV's pitch (3rd DOF in the model), with curves for multiple depth cases. T is the wave period.

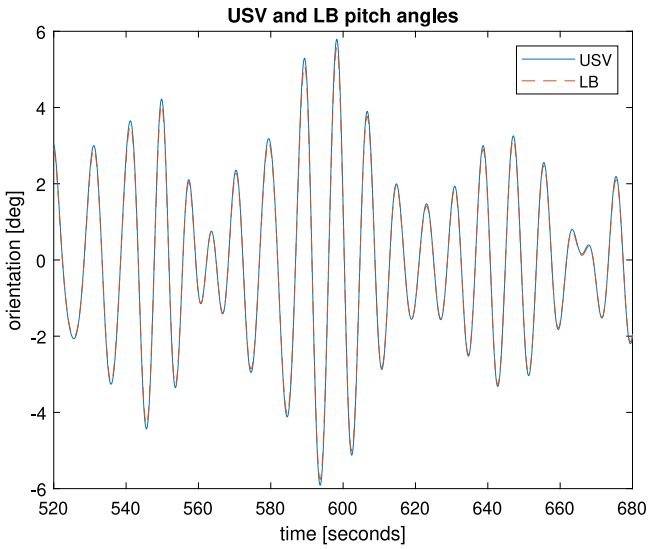

Fig. 8. Pitch angles of USV and latchbeam. Latchbeam is at a depth of $z = 20.20$ m.

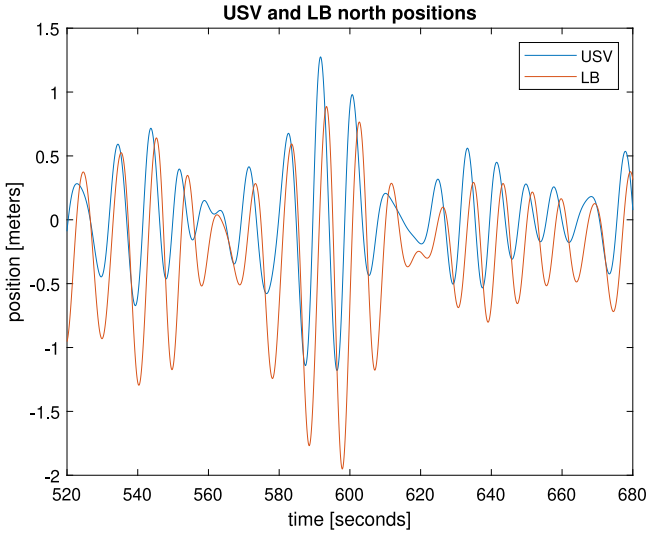

Fig. 9. North position of USV and latchbeam. Latchbeam is at a depth of $z = 20.20$ m.

One important interaction in the model is the coupling between the USV and LB through the wires. Clearly, the cursor wires provide a firm (yet solely tension) vertical guidance, whereas the lateral component of the tension (and also drag and inertia) in the wires exert a soft lateral guidance. Also note that the wire-LB interactions are modeled in the same way as the umbilical-ROV interactions. However, the ROV also includes active control, making analysis of the system much more complicated. Thus, validation of the simpler wire-LB interaction will allow for discussion in the more complicated umbilical-ROV interactions.

Wave-induced motion of the USV will result in LB motion. Specifically, the USV heave motion will result in vertical motion, which ideally is offset by the AHC. The other degrees-of-freedom primarily result in horizontal motion. Fig. 8 shows that the LB pitch angle correlates almost perfectly with the USV pitch angle, which is to be expected given that the wires have positive tension and the points of attack are such that there is a relatively long moment arm between them. When the USV pitches due to a wave, one of the points of attack goes up while the other goes down, creating forces in opposite directions at the points of attachment on the LB. These motions allow gravity to generate a pitching moment in the LB over an arm of over 2 meters (the points of attachment are found in Table 3). The reason for this is that it is assumed that each of the cursor wires are connected to the same winch, and thus work in tandem. Fig. 9 shows the north positions of the objects, corresponding to surge motions because the reference heading is towards north in these simulations. The LB follows the position of the USV, and it can be seen that it is offset slightly to the south and lagging behind, indicating the effect of wire and LB drag caused by ocean current going from north to south. This offset in position and in pitch is increased with larger depth of the latchbeam z_{LB}. As such, the motions of the vessels will be more coupled during the cursor docking scenario, in which we are operating with a depth of $z_{LB} = 5.20$ m.

3. Automatic control systems

In this section the control systems for the USV, ROV and AHC are described. The tuning methods and parameters for the different controllers are also presented.

3.1. USV dynamic positioning - with roll damping

The control system for the USV consists of a roll damping DP controller, implemented through LQR (linear quadratic regulator), Nordvik and Johansen (2022). The controller model consists of the following 10 states: 3 positional states $\boldsymbol{\eta}_{DP} = [x_{cu}, y_{cu}, \psi]^T$, 3 integral states $\dot{\boldsymbol{z}}_{DP} = [x_{cu}, y_{cu}, \psi]^T$ and 4 generalized velocity states in surge, sway, roll and yaw $\boldsymbol{\nu}_{DP} = [u, v, p, r]^T$. The roll rate p is included in order to achieve roll damping. Note that x_{cu} and y_{cu} are the cursor positions with origin at the Earth-fixed reference set-point and x_{cu} axis aligned with the desired heading. Thus the final model is:

$$\dot{\boldsymbol{z}}_{DP} = \boldsymbol{\eta}_{DP} \tag{22a}$$

$$\dot{\boldsymbol{\eta}}_{DP} = \boldsymbol{J}\boldsymbol{\nu}_{DP} \tag{22b}$$

$$\dot{\boldsymbol{\nu}} = \boldsymbol{M}^{-1}(\boldsymbol{B}\boldsymbol{\tau}_c - \boldsymbol{D}\boldsymbol{\nu}_{DP}) \tag{22c}$$

where $\boldsymbol{M}$ and $\boldsymbol{D}$ are the system's mass and linear damping matrices, respectively, and the matrices $\boldsymbol{J}$ and $\boldsymbol{B}$ are given as follows

$$\boldsymbol{J} = \begin{bmatrix} 1 & 0 & 0 & 0 \\ 0 & 1 & -d & 0 \\ 0 & 0 & 0 & 1 \end{bmatrix} \quad \boldsymbol{B} = \begin{bmatrix} 1 & 0 & 0 \\ 0 & 1 & 0 \\ 0 & -l_z & 0 \\ 0 & 0 & 1 \end{bmatrix} \tag{23}$$

Here d represents the distance from the USV's CO to the point of action of the cursor wires, and l_z is the vertical position of the thrusters. The

control vector $\boldsymbol{\tau}_c \in \mathbb{R}^3$ consists of surge, sway and yaw generalized forces. Roll control is thus directly coupled with sway. The model assumes all Euler angles are close to zero, therefore the control error is mapped to body through the $\boldsymbol{J}_{\Theta}^T$ transformation of the full kinematic model, assuming zero roll and pitch and using the current yaw angle. The complete control law also includes a feed-forward term from a nonlinear observer estimating the environmental effects.

The paper assumes the use of state-of-the-art industry standard sensors and state estimators for the position and motion of the USV. The prediction of wave-induced motion of the USV is considered using the method in Nordvik and Johansen (2022) based on the wave force prediction method in Halvorsen et al. (2020). The thrust allocation includes thruster biasing. The focus of this paper is on ROV recovery operability, for detailed derivation of the USV LQR the reader is referred to Nordvik and Johansen (2022).

3.2. ROV control design: LQR vs. PID

The ROV control design study compares both 4-degrees-of-freedom PID (proportional–integral–derivative action) and 6-degrees-of-freedom LQR controllers. The PID controller controls the states surge, sway, heave and yaw independently and is treated as a benchmark. The control law in each DOF is given as

$$\tau_{PID} = K_p x_e + K_i x_i + K_d v_e \tag{24}$$

with x_e being the error in position, x_i being the integral of the error and v_e being the error in generalized velocity.

The LQR control design model includes integral states in order to achieve integral action. The model has a similar structure to the USV model with the notable difference that it includes all 6 degrees of freedom, and linearizes around a yaw angle. This allows for the model to be written in state space form

$$\begin{bmatrix} \dot{\boldsymbol{z}} \\ \dot{\boldsymbol{\eta}} \\ \dot{\boldsymbol{\nu}} \end{bmatrix} = \begin{bmatrix} 0_{6\times6} & I_{6\times6} & 0_{6\times6} \\ 0_{6\times6} & 0_{6\times6} & J \\ 0_{6\times6} & 0_{6\times6} & -M^{-1}D \end{bmatrix} \begin{bmatrix} \boldsymbol{z} \\ \boldsymbol{\eta} \\ \boldsymbol{\nu} \end{bmatrix} + \begin{bmatrix} 0_{6\times6} \\ 0_{6\times6} \\ M^{-1} \end{bmatrix} \boldsymbol{\tau}_{thrust} \tag{25}$$

with the feedback control law given by

$$\boldsymbol{\tau}_{thrust} = -\boldsymbol{K}_{LQR}\tilde{\boldsymbol{x}} \tag{26}$$

The control law uses the LQR gain, obtained from solving the algebraic Riccati equation. Here $\tilde{\boldsymbol{x}} = \boldsymbol{x} - \boldsymbol{x}_{ref}$, with $\boldsymbol{x} = [\boldsymbol{z}^T, \boldsymbol{\eta}^T, \boldsymbol{\nu}^T]^T$, and $\boldsymbol{x}_{ref} = [\boldsymbol{z}_{ref}^T, \boldsymbol{\eta}_{ref}^T, \boldsymbol{\nu}_{ref}^T]^T$. The controller is tuned with the positive definite and diagonal weight matrices $\boldsymbol{Q}_z$, $\boldsymbol{Q}_\eta$, $\boldsymbol{Q}_\nu$, and $\boldsymbol{R}$ in the cost function:

$$V = \int_0^\infty \left(\tilde{\boldsymbol{z}}^T \boldsymbol{Q}_z \tilde{\boldsymbol{z}} + \tilde{\boldsymbol{\eta}}^T \boldsymbol{Q}_\eta \tilde{\boldsymbol{\eta}} + \tilde{\boldsymbol{\nu}}^T \boldsymbol{Q}_\nu \tilde{\boldsymbol{\nu}} + \boldsymbol{\tau}_{thrust}^T \boldsymbol{R} \boldsymbol{\tau}_{thrust} \right) dt \tag{27}$$

Note that the terms $\tilde{\boldsymbol{z}}$, $\tilde{\boldsymbol{\eta}}$, and $\tilde{\boldsymbol{\nu}}$ in the cost function refer to the deviation from the reference states. This cost function is standard in LQR (Bryson and Ho, 1969), and the four terms provides weighted penalties on different important aspects: Zero steady-state error in position, low dynamic error in position, derivative action through weight on velocity, and cost of thruster usage, respectively. Due to the assumption of small roll and pitch angles, with a linearization around yaw, the transformation $\boldsymbol{J}$ becomes a constant kinematic matrix with $\boldsymbol{R}_c$ representing the yaw rotation matrix.

$$\boldsymbol{J} = \begin{bmatrix} \boldsymbol{R}_c & 0_{3\times3} \\ 0_{3\times3} & I_{3\times3} \end{bmatrix} \quad \boldsymbol{R}_c = \begin{bmatrix} \cos(\psi_c) & -\sin(\psi_c) & 0 \\ \sin(\psi_c) & \cos(\psi_c) & 0 \\ 0 & 0 & 1 \end{bmatrix} \tag{28}$$

3.2.1. Modifications

For the LQR, a gain scheduling algorithm was implemented to allow for variations in heading angle. The LQR gain matrices for pre-defined heading angles ψ_c were pre-computed and stored in a look-up-table with increments of 0.5°, 720 in total. Should the ROV deviate by $\pm\psi_n$ from the reference heading, or half of that $\pm\psi_n/2$ from a linearization heading angle which is not the USV reference, a new gain matrix is extracted from the look-up-table and the relinearization heading updated. The relinearization threshold ψ_n was set to 5°.

Table 4
Gains for the ROV PD controller for latchbeam and cursor docking.

Gain	Wires	Umbilical
P	1	0.9
D	1.4	1.4

During LB docking the control objective is for the ROV to track the LB, and thus the LB's position and velocity is used to generate references. During cursor docking the combined LB and ROV object tracks the cursor. The surge and sway states are most important, and heave is neglected since the combined object will be pulled up by winches that dominate the force balance since the coupled LB and ROV object has substantially negative buoyancy. This assumption has been validated though computational readouts showing positive tension throughout operation. It was found beneficial to switch off the integral action in heave for both controllers (PID and LQR) in both docking modes to prevent integrator windup and thruster saturation stemming from different small static error sources in heave that is not possible or desirable to compensate for. For example, during cursor docking, the combined ROV and LB object was observed to be consistently under the reference, due to the LB weight stretching the cursor wires. The thrusters do not have enough control authority to lift up the LB, eventually resulting in saturation if integral windup happens. During LB docking the ROV's umbilical force is included, and the controller could end up working against the umbilical if the LB is at a depth which results in a heave reference larger than the nominal length of the umbilical, again resulting in buildup of thrust and high umbilical tension. It was therefore concluded that integral action in heave is not desired.

In order to avoid slack in the umbilical during LB docking, a virtual weight by means of a constant downwards thrust from the ROV was implemented. This is meant to induce a bias in the tension of the umbilical, ensuring a safety margin to prevent slack. This was set to about 50% of the ROV's thrust capabilities in heave, or 5 kN, assuring a sufficient margin while still allowing for dynamic control authority in heave.

3.3. Active heave compensation (AHC)

During LB docking, the AHC scheme is meant to decouple the LBs's vertical motion from the surface wave induced vertical motion of the USV. When the USV moves up with a wave, the cursor wires pull on the LB when there is no AHC. This makes the tracking problem of the ROV harder, but more importantly, it results in lower tension in the cursor wires when the USV moves down again. The AHC system consists of winches which adjust the length of the cursor wires based on the heave position and velocity of the USV. The winches are modeled as first order dynamic systems with the transfer function

$$\Delta l_{W*} = \frac{K_W}{T_W s + 1} u_W \tag{29}$$

where $T_W = 1.5915$ s is the time constant of the winch, K_W is the gain, Δl_{W*} is the rate limited change of wire length (max rate set to 0.6 m/s) and u_W is a control input given by

$$u_W = -K_p z^n - K_d w^b \tag{30}$$

with z^n and w^b being the USV's heave position and velocity in NED and BODY, respectively. The same AHC was also implemented for the umbilical, with the same winch and rate limitation but different gains in order to account for the slower dynamics of the latchbeam docking compared to the cursor docking. The gains are given in Table 4.

Table 5
LQR state and control weights, control effect gains and USV feed-forward gains for latchbeam docking/cursor docking.

State	LQR Q		LQR R	
	USV	ROV	USV	ROV
x	1	3800	1	0.001
y	1	3000	1	0.001
z		1200/1		0.001
ϕ	$10(\frac{180}{pi})^2$	$0.1\ (\frac{180}{pi})^2$	0.25	0.001
θ		$0.1\ (\frac{180}{pi})^2$		0.001
ψ	$(\frac{180}{pi})^2$	$0.1\ (\frac{180}{pi})^2$	$\frac{1}{9^2}$	0.001
	Control effects gains			
z	10^6	1		
η	10^8	70		
ν	10^8	85		
	USV feedforward gains			
x	0.25			
y	0.5			
ψ	0.1			

3.4. Tuning of the controllers

The LQR controllers use a transparent tuning scheme. Instead of tuning each state in the high dimensional state space, a weight for each degree-of-freedom of the vessel is tuned, and an effects gain for the integral, positional and velocity state is used to tune the effects themselves. This reduces the complexity of the tuning procedure. The weight matrices for a 6 DOF LQR, like the ROV LQR, with this tuning scheme then look as presented in Eq. (31). Note that for the USV LQR controller the weight matrices are reduced in dimension to reflect the reduced number of controlled states. So the matrices are $\boldsymbol{Q_z}^{3\times3}$, $\boldsymbol{Q_\eta}^{3\times3}$, $\boldsymbol{Q_\nu}^{4\times4}$ with identical structure to the ones in Eq. (31).

$$Q_z = q_z \cdot \text{diag}\{q_x \quad q_y \quad q_z \quad q_\phi \quad q_\theta \quad q_\psi\} \tag{31a}$$

$$Q_\eta = q_\eta \cdot \text{diag}\{q_x \quad q_y \quad q_z \quad q_\phi \quad q_\theta \quad q_\psi\} \tag{31b}$$

$$Q_\nu = q_\nu \cdot \text{diag}\{q_x \quad q_y \quad q_z \quad q_\phi \quad q_\theta \quad q_\psi\} \tag{31c}$$

The ROV LQR controller tuning was analyzed and verified through frequency response methods, utilizing the linear nature of the controller. Bode plots of the transfer functions from reference and disturbance to position were used. While it is based on classical control engineering found in any basic text book, the method is outlined in detail in Section 4.5.3 of Lysthaug (2022).

Preliminary results with the PID can be found in Landstad et al. (2021). Its tuning was updated in this paper since the models have been improved. It can be observed that the PID control law has a structure very similar to that of the LQR. Thus, once a tuning for the LQR and therefore a $\boldsymbol{K}_{lqr} \in \mathbb{R}^{6\times18}$ matrix is obtained, the diagonal elements in the 6×6 blocks responsible for proportional, integral and derivative actions could be extracted and used as gains in the PID for the relevant states. This is a transparent tuning procedure that leads to a stable PID, which is directly comparable with the LQR. This comparison allows us to asses if the LQR is able to exploit its off-diagonal gain components to improve performance.

The AHC systems for both wires and umbilical were tuned through an empirical trial-and-error approach, which is feasible for such simple controllers. An overview of the gains is presented in Tables 5 and 6.

4. Results and discussion

In this section results from simulations are used to study several important factors that influence the operability, by evaluating the performance of the control systems design from both a qualitative and a quantitative perspective. In Sections 4.1 and 4.2, the LB docking case is analyzed at one specific sea state: $H_s = 3.5$ m for significant wave height and $T_m = 9.5$ s for the peak wave period, which corresponds to a typical North Sea condition with MSO sea state code 5 (Rough). All the simulations were ran with the same random generator seed for the wave realization. The wind speed is calculated as a function of the significant wave height to be $V_w = 11.6$ m/s, and the speed of the current is $V_c = 0.3$ m/s which is typical for parts of the North Sea.

Table 6
Gains for the ROV PID controller for latchbeam and cursor docking.

State	Latchbeam docking			Cursor docking		
	P	I	D	P	I	D
	$\cdot10^4$	$\cdot10^3$	$\cdot10^3$	$\cdot10^4$	$\cdot10^3$	$\cdot10^3$
x	1.8759	1.9494	2.1596	1.8917	1.9494	2.3113
y	1.8759	1.7321	2.0600	1.6982	1.7321	2.2011
z	1.3145	0	1.6862	0.0500	0	0.2178
ψ	0.5591	0.5730	0.7005	0.5662	0.5730	0.7705

In general the LB docking scenario will be used for qualitative analysis of the physical phenomena at play and the way they interact with the control systems. Section 4.3 focuses on cursor docking and compares the performance of the PID and LQR controllers. A statistical evaluation of the control systems for the ROV is performed for many sea states and a sensitivity analysis for the direction of the incoming environmental forces is performed, thus providing quantitative metrics. The mean environmental forces all come from North, which is also the desired heading direction in the simulations, unless otherwise specified. The surge direction is therefore close to the direction towards North.

The operability criteria, which are used to evaluate the performance of the system, are summarized and put into context below:

- During LB docking, the ROV tracking accuracy in xyz is important. Typically the tracking objective is an average Euclidean error below 10 cm.
- During cursor docking, tracking in z is neglected due to the assumption that the combined ROV-LB object will be slowly hoisted by the umbilical winch. Typically, the tracking accuracy objective can be relaxed to an average error below 20 cm in xy.
- Avoiding slack (no tension) in the cursor wires and umbilical is a critical operability constraint. It both prevents the risk of wire snap, and ensures that the tensioned wires will provide a level of guiding of the LB and ROV. For the cursor wires a minimum tension of 0.5 kN is considered safe.
- The umbilical also has a maximum tension. As a simple rule of thumb, a design constraint is set as 1/8th of the tensile strength of the umbilical, which is roughly 10 kN for the simulated umbilical.

The system is required to achieve small tracking errors in limited periods which are opportune for final docking. In the total system such periods are expected to be identified through wave prediction using e.g. a wave radar. Hence, this paper will consider average tracking errors over relatively long simulation periods of 1000 s. This makes the analysis here more conservative, as peaks in errors are also included in the computation. In a realistic operation the system is not required to perform well during these peaks, as they will not be identified as opportune docking periods.

4.1. AHC verification

The cursor wires are kept tensioned by the weight of the LB. This induces tension in the wires and prevents slack. The heave motion of the LB roughly follows the USV, with the amplitude being reduced as a function of how agile the AHC system is. Fig. 10 shows that the AHC achieves significant reduction of the LB motion relative to the Earth, when operating at sufficiently deep waters. In this case, the simulation is done with the LB placed 20.2 m below the USV. Furthermore, the standard deviations in the heave motions were found to be $z_{usv,std} = 0.4381$ and $z_{lb,std} = 0.0553$ for the USV and latchbeam respectively.

Fig. 11 shows the tension in both wires compared to the minimum tension limit given the operability criteria. The tension is kept well

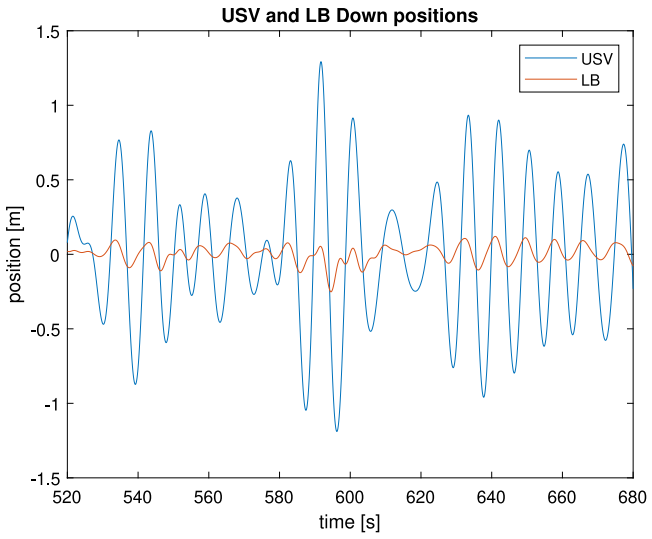

Fig. 10. Heave position of USV and latchbeam. The heave for latchbeam is mean centered.

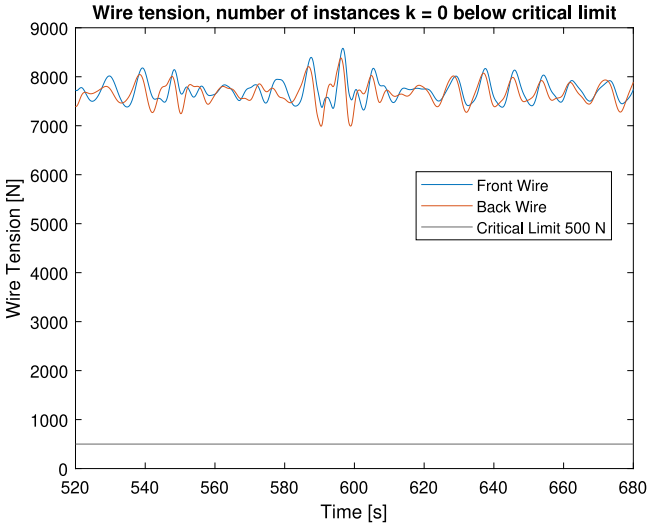

Fig. 11. Wire tension and the critical limit for wire tension. The results confirm that the wires are always taut with some minimum tension margin.

over the margin throughout the simulation with a mean tension of $T_1 = 7728\ N$ for the front wire and $T_2 = 7676\ N$ for the back wire. For this simulation the probable minimum tension in the wires was also $T_{min} = 6467$ N, adhering to the operability criteria.

4.2. Latchbeam docking

According to industry practice, the umbilical provides a valuable contribution to hoisting the neutrally buoyant ROV during LB docking. Like the cursor wires, slack is a problem with the umbilical. However, unlike the cursor wires, the umbilical is not designed to be fully weight bearing, so maximum tension is also a concern. Table 7 contains the results of 4 simulations with different umbilical/control configurations, which confirms the role the umbilical plays in guiding the ROV. Both the use of the umbilical as well as active roll damping in the USV have a positive effect on the tracking accuracy. It can be seen that the umbilical provides a benefit both in vertical and horizontal tracking, while the 2 cm improvement in tracking accuracy due to the USV roll damping are mainly helping with horizontal tracking.

Table 7
Euclidean distance errors [m] for 4 different configurations of umbilical and active control. Umbilical, tensioned refers to the umbilical being used to hoist the ROV.

xyz	ϕ damp ON	ϕ damp OFF
Umbilical, tensioned	0.0759	0.0915
Umbilical, no tension	0.0838	0.1036
xy	ϕ damp ON	ϕ damp OFF
Umbilical, tensioned	0.0569	0.0753
Umbilical, no tension	0.0684	0.0870

A typical tracking performance for the system during latchbeam docking is seen in Fig. 12. An animation of parts of the simulation is found in Tran (2023b). The scenario is $H_s = 3.5$ m, $T_p = 9.5$ s and ROV is at an average depth of 20.2 m. The error varies due to the motion of the USV and the way it affects the LB and ROV. The biggest challenges are in North/surge and Down/heave tracking. These coincide with the USV moving up and down with the waves, and pitching which was shown to affect the North/surge position of the LB significantly. The average Euclidean error in xyz for the entire period here is 0.076 m, which is within the operational requirements. However, the errors exceed at times the operability criteria of 10 cm, with the probable maximum error being 23 cm. One must therefore be able to identify periods of favorable docking, where the tracking is sufficiently below the criteria. Between $t = 290$ s and $t = 310$ s, the average Euclidean tracking error is down to 0.039 m. As the docking procedure will take a few seconds once an opportunity is identified, this tracking performance over a period of 20 s should prove satisfactory.

4.3. Cursor docking

During cursor docking the ROV is rigidly attached to the LB, which is slowly hoisted up with the cursor wires. Compared to the LB docking case, the tension margin is a lot higher, which lowers the risk of slack significantly due to the large weight of the LB. The cursor wires do not have as restrictive maximum tension requirement as the umbilical. Additionally, there are two of them which allows for the load to be distributed. Finally, they stabilize the combined ROV and LB object. An animation of such a simulation is found in Tran (2023a). The scenario is $H_s = 3.5$ m, $T_p = 9.5$ s and ROV is at an average depth of 5.2 m.

During the previous simulations in this paper, the USV had a heading reference towards North, where the mean environmental forces are coming from. In realistic scenarios one must expect some further variations or operational constraints that may prevent the optimal heading to be chosen. Therefore, a sensitivity analysis with respect to the heading relative to the mean environmental forces is in order. In this analysis, the mean environmental forces are coming from North while the USV is given heading references in increments of 5°, starting at −45° and ending at 45°. The results are presented in Figs. 13 and 14 showing average xy error and average thrust respectively. Both controllers manage to keep tension above the critical limits at all headings. The LQR performs better for all the headings, with slightly smaller error than the PID controller. However, the LQR also requires more thrust than the PID for most of the angles. Regardless, both the controllers are well within operational requirements with a average error norm of 5.47 cm and 6.08 cm for the LQR and PID controller respectively.

Tables 8–11 and 12–15 show some statistical results for the PID and LQR controllers respectively in cursor docking for 18 different sea states. Here the maximum error norm refers to a probable maxima of error given the seed for the wave realizations. The minimum wire tension is also a probable minima for the seed. The simulation period for all the simulations is 1000 s. It can be seen that the differences observed in the controllers are marginal when it comes to error. The similarity between the PID and LQR controllers likely stems from the

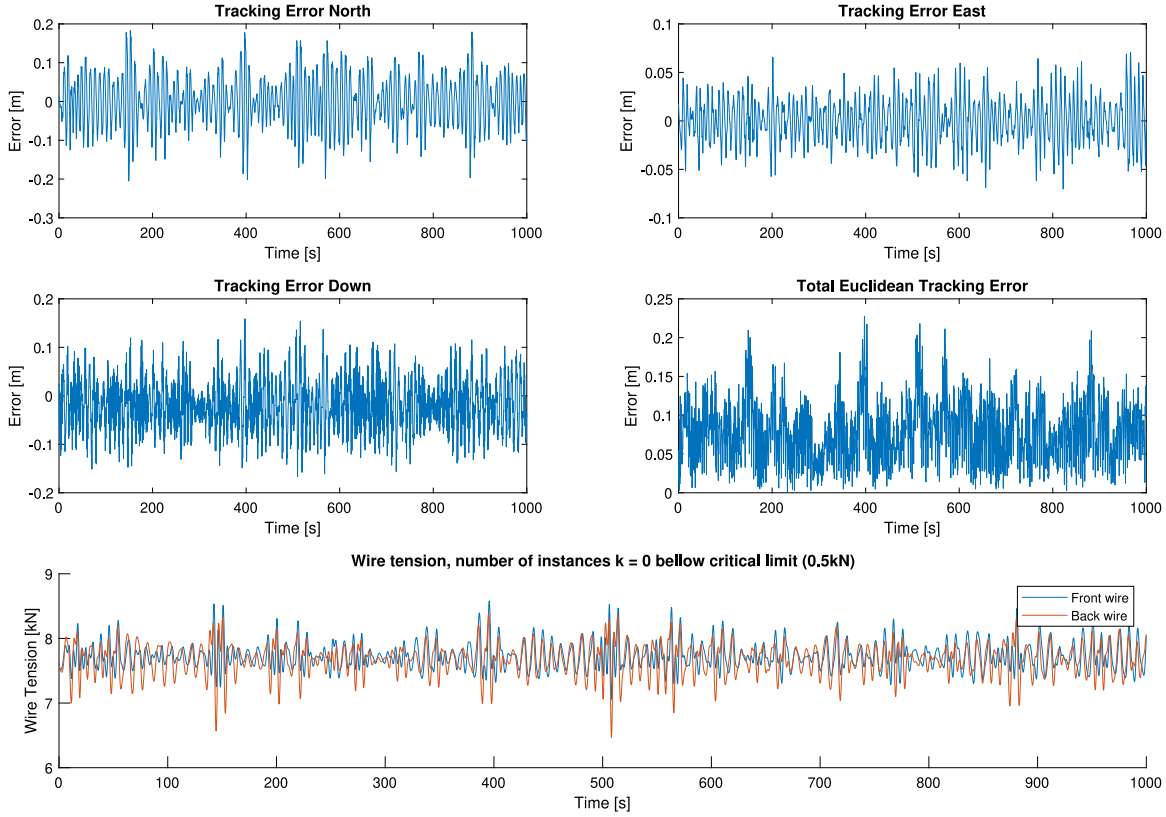

Fig. 12. Tracking errors in translational degrees-of-freedom during latchbeam docking, and wire tension. Total Euclidean Tracking error refers to the norm of the xyz error.

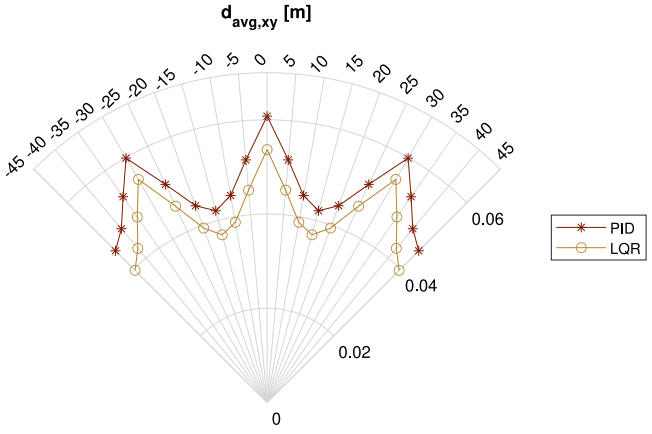

Fig. 13. Average tracking errors in translational degrees of freedom, as well as Euclidean norm of the xy error.

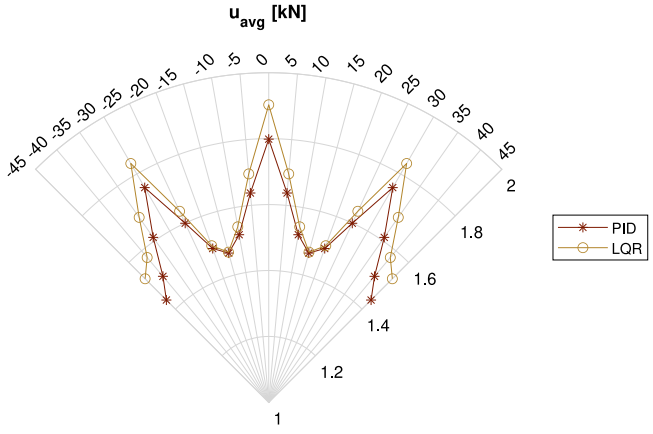

Fig. 14. Polar plot showing the average thrust expended by the controllers.

way the PID was tuned. Taking the diagonal elements of the LQR gains results in a very similar controller, as those are the dominant gains. The PID controller maintains higher minimum tension for most of the sea states. Both controller adheers to the criteria of wire tension above 0.5 kN.

5. Conclusions

A numerical simulation model for ROV recovery from a small USV is presented, validated and used in analyzing operability criteria. In Section 4.1 it was shown that simulations fit with the physical intuition of how the system generally should perform, verifying the simulator and allowing for further discussion on physical phenomena using results from simulation. As discussed in Sections 4.2 and 4.3, simulation is used to verify that the tracking performance of the ROV satisfies the operability criteria, with the positive benefits of USV roll damping and tension in the umbilical being demonstrated. Furthermore, an agile AHC and ROV heave controller can allow for decoupling of the USV and ROV, yielding good tracking results. There are indications that active control alone can assure tracking errors well within operability criteria without the use of the umbilical to hoist the ROV. This which might allow for a redesign of the role of the umbilical in the final product.

In the statistical analyses performed in Section 4.3 the LQR showed more robust results than the PID counterpart, which was tuned using the LQR's diagonal elements. Note that the PID control has no active

roll and pitch control at all. This might not be a problem in practice, as these states will not be identified as opportune for docking. However, it is reasonable to not use roll and pitch integral action in the LQR during cursor docking. In most cases the angles of the ROV-LB object are dominated by the forces from the cursor wires. The USV is additionally advised to take a heading against the environmental forces in order to make the task of the ROV controller easier during docking.

Standard sensors for the USV, LB and ROV were used in the simulations, together with a wave-force prediction for the USV based on inertial measurements (Halvorsen et al., 2020; Nordvik and Johansen, 2022). This could possibly be improved by the use of wave radar and other innovative sensing systems and dynamic models, involving also prediction of the latchbeam and ROV motions.

We recall that the objective of this paper was *not* to present the complete design of a control system for the ROV recovery operation. The various elements of the control design framework have indeed been published separately, and analyzed individually. Instead, this paper studies how the choice of control algorithm and its tuning parameters strongly influences the operability metrics (primarily tracking error and wire tension). This indicates that the control system elements cannot be simplified too much when analyzing operability of such critical operations. It shows that numerical system simulation that integrates all physical elements and control systems is an effective method to verify operability from a systems perspective. It would be useful in further studies to consider the possibility of applying this model in practice and evaluate its effectiveness in various operating conditions.

CRediT authorship contribution statement

Celine Tran: Methodology, Software, Validation, Investigation, Writing – original draft, Visualization. **Ivan Gushkov:** Methodology, Software, Validation, Investigation, Writing – original draft, Visualization. **Kristoffer Nordvik:** Conceptualization, Methodology, Software, Validation, Investigation, Writing – original draft, Visualization. **Simen T. Røang:** Methodology, Software, Validation, Investigation, Writing – original draft, Visualization. **Simen B. Lysthaug:** Methodology, Software, Validation, Investigation, Writing – original draft, Visualization. **Babak Ommani:** Methodology, Validation, Resources, Writing – review & editing. **Thor I. Fossen:** Methodology, Software, Validation, Writing – review & editing. **Vahid Hassani:** Validation, Resources, Writing – review & editing, Project administration, Funding acquisition. **Vidar Smines:** Conceptualization, Validation, Resources, Writing – review & editing, Visualization, Project administration, Funding acquisition. **Tor A. Johansen:** Conceptualization, Methodology, Validation, Resources, Writing – original draft, Visualization, Supervision, Project administration, Funding acquisition.

Declaration of competing interest

The authors declare that they have no known competing financial interests or personal relationships that could have appeared to influence the work reported in this paper.

Data availability

The data that has been used is confidential.

Acknowledgments

We thank the ROV Revolution project team at Kongsberg Maritime, Reach Subsea, SINTEF Ocean and NTNU.

Table 8
Average surge-sway tracking error [m] at 18 different sea states for the PID controller.

H_s [m]	T_m [s]						
	6.5 s	7.5 s	8.5 s	9.5 s	10.5 s	11.5 s	12.5 s
0.5 m	0.05	0.05	0.05				
1.5 m		0.06	0.05	0.04			
2.5 m			0.04	0.04	0.05		
3.5 m				0.06	0.06	0.05	
4.5 m				0.05	0.06	0.06	
5.5 m					0.07	0.06	0.05

Table 9
Maximum surge-sway tracking error [m] at 18 different sea states for the PID controller.

H_s [m]	T_m [s]						
	6.5 s	7.5 s	8.5 s	9.5 s	10.5 s	11.5 s	12.5 s
0.5 m	0.35	0.37	0.38				
1.5 m		0.39	0.34	0.31			
2.5 m			0.27	0.25	0.25		
3.5 m				0.32	0.42	0.49	
4.5 m				0.55	0.62	0.69	
5.5 m					0.75	0.64	0.56

Table 10
Average thrust [kN] at 18 different sea states for the PID controller.

H_s [m]	T_m [s]						
	6.5 s	7.5 s	8.5 s	9.5 s	10.5 s	11.5 s	12.5 s
0.5 m	1.44	1.50	1.61				
1.5 m		1.75	1.60	1.50			
2.5 m			1.47	1.52	1.64		
3.5 m				1.80	1.71	1.64	
4.5 m				1.60	1.59	1.62	
5.5 m					1.67	1.53	1.42

Table 11
Minimum wire tension [kN] at 18 different sea states for the PID controller.

H_s [m]	T_m [s]						
	6.5 s	7.5 s	8.5 s	9.5 s	10.5 s	11.5 s	12.5 s
0.5 m	6.11	6.62	3.71				
1.5 m		4.98	5.78	3.38			
2.5 m			4.51	5.08	3.28		
3.5 m				4.01	4.42	2.40	
4.5 m				3.14	3.45	2.35	
5.5 m					2.69	3.17	5.83

Table 12
Average surge-sway tracking error [m] at 18 different sea states for the LQR, with color coding indicating improvement (green) or decrease (red) in performance with respect to the PID controller.

	T_m (s)						
H_s(m)	6.5 s	7.5 s	8.5 s	9.5 s	10.5 s	11.5 s	12.5 s
0.5	0.04	0.04	0.05				
1.5		0.05	0.05	0.04			
2.5			0.04	0.04	0.05		
3.5				0.05	0.05	0.05	
4.5				0.04	0.04	0.05	
5.5					0.05	0.04	0.04

Appendix. Cursor docking - statistical simulation results

Tables 8–15 summarizes statistics about the performance evaluation in the most relevant sea states, and with the USV heading towards the mean environmental forces (North).

Table 13
Maximum surge-sway tracking error [m] at 18 different sea states for the LQR, with color coding indicating improvement (green) or decrease (red) in performance with respect to the PID controller.

	T_m (s)						
H_s(m)	6.5 s	7.5 s	8.5 s	9.5 s	10.5 s	11.5 s	12.5 s
0.5	0.15	0.16	0.20				
1.5		0.24	0.20	0.17			
2.5			0.18	0.21	0.24		
3.5				0.26	0.25	0.23	
4.5				0.21	0.22	0.22	
5.5					0.23	0.20	0.18

Table 14
Average thruster [kN] usage at 18 different sea states for the LQR, with color coding indicating decreased (green) or increased (red) thruster usage with respect to the PID controller.

	T_p (s)						
H_s(m)	6.5 s	7.5 s	8.5 s	9.5 s	10.5 s	11.5 s	12.5 s
0.5	1.53	1.57	1.69				
1.5		1.84	1.64	1.51			
2.5			1.47	1.54	1.70		
3.5				1.90	1.78	1.68	
4.5				1.64	1.65	1.72	
5.5					1.82	1.65	1.52

Table 15
Minimum wire tension [kN] at 18 different sea states for the LQR, with color coding indicating increased (green) or decreased (red) minimum wire tension compared to the PID controller.

	T_p (s)						
H_s(m)	6.5 s	7.5 s	8.5 s	9.5 s	10.5 s	11.5 s	12.5s
0.5	6.29	6.82	3.57				
1.5		4.99	5.88	3.04			
2.5			4.38	5.07	2.72		
3.5				3.65	4.28	1.71	
4.5				2.30	2.93	1.59	
5.5					2.00	2.45	5.97

References

Acero, W.G., Gao, Z., Moan, T., 2017. Methodology for assessment of the allowable sea states during installation of an offshore wind turbine transition piece structure onto a monopile foundation. J. Offshore Mech. Arct. Eng. 139 (6).

Anon, 2011. Modelling and Analysis of Marine Operations. Tech. Rep. DNV-RP-H103, Det Norske Veritas.

Berg, T., Selvik, Ø., Berge, B., 2015. Defining operational criteria for offshore vessels. In: Ehlers, S., et al. (Eds.), Maritime-Port Technology and Development. Taylor & Francis Group, London.

Bryson, A.E., Ho, Y.-C., 1969. Applied Optimal Control. Blaisdell Publishing Company, Waltham.

Cummins, W.E., 1962. The Impulse Response Function and Ship Motions. Tech. Rep., David Taylor Model Basin–DTNSRDC.

Faltinsen, O.M., 1990. Sea Loads on Ships and Offshore Structures. Cambridge University Press Cambridge.

Fossen, T.I., 2021. Handbook of Marine Craft Hydrodynamics and Motion Control. Wiley.

Fossen, T.I., Perez, T., 2004. Marine systems simulator (MSS). URL https://github.com/cybergalactic/MSS.

Fossen, T., Perez, T., 2008. Joint identification of infinite-frequency added mass and fluidmemory models of marine structures. Model. Identif. Control 29, 93–102.

Guachamin Acero, W., Li, L., Gao, Z., Moan, T., 2016. Methodology for assessment of the operational limits and operability of marine operations. Ocean Eng. 125, 308–327.

Halvorsen, H.S., Øveraas, H., Landstad, O., Smines, V., Fossen, T.I., Johansen, T.A., 2020. Wave motion compensation in dynamic positioning of small autonomous vessels. J. Mar. Sci. Technol. 26, 693–712.

Johansen, T.A., Fossen, T.I., Sagatun, S.I., Nielsen, F.G., 2003. Wave synchronizing crane control during water entry in offshore moonpool operations - experimental results. IEEE J. Ocean. Eng. 29, 720–728.

Journée, J., Massie, W., 2001. Offshore Hydromechanics. Delft University of Technology, Delft, Netherlands.

Kristiansen, E., Hjulstad, A., Egeland, O., 2006. State-space representation of radiation forces in time-domain vessel models. Model. Identif. Control 27, 23–41.

Landstad, O., Halvorsen, H., Øveraas, H., Smines, V., Johansen, T.A., 2021. Dynamic positioning of ROV in the wave zone during launch and recovery from a small surface vessel. Ocean Eng. 235, 109382.

Levy, E.C., 1959. Complex-curve fitting. IRE Trans. Autom. Control AC-4 (1), 37–43.

Li, L., Parra, C., Zhu, X., Ong, M.C., 2020. Splash zone lowering analysis of a large subsea spool piece. Mar. Struct. 70, 102664.

Lysthaug, S.B., 2022. Dynamic Positioning of a Remotely Operated Vehicle During Launch and Recovery (Master's thesis). Norwegian University of Science and Technology.

Nordvik, K., Johansen, T.A., 2022. On compensation for wave-induced roll in dynamic positioning control. J. Mar. Sci. Technol. 106.

Ommani, B., Kristiansen, T., Berget, K., 2018. Investigating a simplified model for moonpool piston mode response in irregular waves. In: Proc. International Conference on Ocean, Offshore and Arctic Engineering. http://dx.doi.org/10.1115/OMAE2018-78352.

Perez, T., Fossen, T.I., 2009. A matlab toolbox for parametric identification of radiation-force models of ships and offshore structures. Model. Identif. Control 30 (1), 1–15.

Tran, C., 2023a. Animation of simulation - Cursor docking. URL https://folk.ntnu.no/torarnj/cursor_docking.avi.

Tran, C., 2023b. Animation of simulation - Latchbeam docking. URL https://folk.ntnu.no/torarnj/latchbeam_docking.avi.

WAMIT, 2020. Wamit© user manual version 7.3. https://www.scribd.com/document/255163083/WAMIT-V70-Manual. (Accessed 16 April 2020).